RESEARCH ARTICLE | DECEMBER 04 2024

Numerical simulations of laser-driven experiments of ion acceleration in stochastic magnetic fields ⊕

K. Moczulski ✉ ⓘ ; H. Wen ⓘ ; T. Campbell ⓘ ; A. Scopatz ⓘ ; C. A. J. Palmer ⓘ ; A. F. A. Bott ⓘ ;
C. D. Arrowsmith ⓘ ; K. A. Beyer ⓘ ; A. Blazevic ⓘ ; V. Bagnoud ⓘ ; S. Feister ⓘ ; J. Halliday ⓘ ;
O. Karnbach ⓘ ; M. Metternich ⓘ ; H. Nazary ⓘ ; P. Neumayer ⓘ ; A. Reyes ⓘ ; E. C. Hansen ⓘ ;
D. Schumacher ⓘ ; C. Spindloe ⓘ ; S. Sarkar ⓘ ; A. R. Bell ⓘ ; R. Bingham ⓘ ; F. Miniati ⓘ ;
A. A. Schekochihin ⓘ ; B. Reville ⓘ ; D. Q. Lamb; G. Gregori ⓘ ; P. Tzeferacos ⓘ

Check for updates

View Online

Export Citation

Articles You May Be Interested In

Insensitivity of a turbulent laser-plasma dynamo to initial conditions

Matter Radiat. Extremes (June 2022)

Numerical simulations of laser-driven experiments of ion acceleration in stochastic magnetic fields 🔵EP

K. Moczulski,[1,a] 🔵 H. Wen,[1] 🔵 T. Campbell,[2] 🔵 A. Scopatz,[1] 🔵 C. A. J. Palmer,[3] 🔵 A. F. A. Bott,[2] 🔵
C. D. Arrowsmith,[2] 🔵 K. A. Beyer,[4] 🔵 A. Blazevic,[5] 🔵 V. Bagnoud,[5] 🔵 S. Feister,[6] 🔵 J. Halliday,[2,7] 🔵 O. Karnbach,[2] 🔵
M. Metternich,[5] 🔵 H. Nazary,[8] 🔵 P. Neumayer,[5] 🔵 A. Reyes,[1] 🔵 E. C. Hansen,[1] 🔵 D. Schumacher,[5] 🔵 C. Spindloe,[7] 🔵
S. Sarkar,[2] 🔵 A. R. Bell,[2] 🔵 R. Bingham,[7,9] 🔵 F. Miniati,[2] 🔵 A. A. Schekochihin,[2] 🔵 B. Reville,[4] 🔵 D. Q. Lamb,[10]
G. Gregori,[2] 🔵 and P. Tzeferacos[1] 🔵

AFFILIATIONS

[1]University of Rochester, Rochester, New York 14627, USA
[2]University of Oxford, Oxford OX1 3PU, United Kingdom
[3]Queens University Belfast, Belfast BT7 1NN, United Kingdom
[4]Max-Planck-Institut für Kernphysik, Saupfercheckweg 1, D-69117 Heidelberg, Germany
[5]GSI Helmholtzzentrum für Schwerionenforschung GmbH, D-64291 Darmstadt, Germany
[6]California State University Channel Islands, Camarillo, California 93012, USA
[7]STFC Rutherford Appleton Laboratory, Didcot OX11 0QX, United Kingdom
[8]Technische Universität Darmstadt, D-64289 Darmstadt, Germany
[9]Department of Physics, University of Strathclyde, Glasgow G4 0NG, United Kingdom
[10]University of Chicago, Chicago, Illinois 60637, USA

[a]Author to whom correspondence should be addressed: kmoczuls@ur.rochester.edu

ABSTRACT

We present numerical simulations used to interpret laser-driven plasma experiments at the GSI Helmholtz Centre for Heavy Ion Research. The mechanisms by which non-thermal particles are accelerated in astrophysical environments, e.g., the solar wind, supernova remnants, and gamma ray bursts, is a topic of intense study. When shocks are present, the primary acceleration mechanism is believed to be first-order Fermi, which accelerates particles as they cross a shock. Second-order Fermi acceleration can also contribute, utilizing magnetic mirrors for particle energization. Despite this mechanism being less efficient, the ubiquity of magnetized turbulence in the universe necessitates its consideration. Another acceleration mechanism is the lower-hybrid drift instability, arising from gradients of both density and magnetic field, which produce lower-hybrid waves with an electric field that energizes particles as they cross these waves. With the combination of high-powered laser systems and particle accelerators, it is possible to study the mechanisms behind cosmic-ray acceleration in the laboratory. In this work, we combine experimental results and high-fidelity three-dimensional simulations to estimate the efficiency of ion acceleration in a weakly magnetized interaction region. We validate the FLASH magneto-hydrodynamic code with experimental results and use OSIRIS particle-in-cell code to verify the initial formation of the interaction region, showing good agreement between codes and experimental results. We find that the plasma conditions in the experiment are conducive to the lower-hybrid drift instability, yielding an increase in energy $\Delta\mathscr{E}$ of $\sim 264\,\text{keV}$ for 242 MeV calcium ions.

I. INTRODUCTION

Cosmic rays have been studied for well over a century, and it was only in the 1910s that we realized they came not from the Earth's crust, but instead bombarded the Earth's upper atmosphere.[1,2] Despite more than a century of investigation, both the sites of acceleration[3] and plasma processes[4] that generate the range of energies measured in cosmic rays remain open questions and, thus, topics of active research.

The energization mechanisms that are expected to operate in astrophysical systems rely on collisionless interaction with the electric and magnetic fields supported by the tenuous plasmas typical of these

16 December 2024 09:26:15

environments. The most widely invoked acceleration mechanism in astrophysics is diffusive shock acceleration,[5–8] an example of a first-order Fermi mechanism. Two key requirements for such mechanisms to occur are the ability to lift a subset of particles from the thermal gas to energies where they decouple from the bulk flow, and a scattering process that can sustain the acceleration and lead to the formation of a non-thermal component, i.e., not simply a heating process. Both processes rely on the interplay between particle transport and plasma turbulence. Large-scale kinetic simulations of shocks suggest that the diffusive shock acceleration process can be efficient under a broad range of plasma environmental conditions.[9] Moreover, satellite measurements present compelling evidence for energization due to interactions with whistler[10] as well as lower-hybrid[11] waves in the case of electrons, or ion-cyclotron modes[12] in the case of ions. These provide possible routes to injecting particles into the shock acceleration process. More recently, laboratory experiments and simulations of collisionless shocks have shown electron and ion spectra consistent with shock acceleration predictions.[13–15]

That said, particle acceleration does not occur only at shocks. The acceleration mechanism originally proposed by Fermi[16] posited that particles are accelerated through repeated interaction with moving magnetic field structures. In the original picture, charged particles propagating through a magnetized medium can interact with magnetic fields, the latter acting as mirrors changing the particle energy proportional to the mirror velocity. If a mirror is moving toward a particle, it will result in an energy increase. Conversely, if receding, the particle gets decelerated. Unlike at shocks, where there exists a clear preferred direction, here, the mirrors are assumed to be randomly oriented and the resulting energy gain averaged over many interactions is thus second order in the mirrors' velocity.[17,18] While less efficient than first-order Fermi, the large extent of interstellar and intracluster mediums can increase the likelihood of meaningful contributions from second-order Fermi acceleration. Hence, it is expected to modify, rather than dominate, the cosmic ray spectrum.[19] Despite detailed theoretical studies,[20,21] laboratory evidence of second-order Fermi ion acceleration has remained elusive.

Inhomogeneous environments, which are common in astrophysical contexts, can also lead to instabilities. The lower-hybrid drift instability, which develops from misaligned gradients of density and magnetic field, is one such example.[22] When these gradients are present, lower-hybrid waves can develop, generating electric fields that in turn accelerate charged particles. Theoretical models have been proposed to explain the hard x-ray tail emission in Cassiopeia, arguing the lower-hybrid drift instability provides the necessary acceleration for electrons.[23] Simulations have expanded upon the quasi-linear theoretical framework,[22] and have demonstrated that electrons can be self-consistently accelerated.[24] Measurements of accelerated auroral electrons have been analyzed, showing lower-hybrid waves as the cause of acceleration.[25] Space probes have measured the lower-hybrid drift instability in the magnetotail current sheet,[26] showing that lower-hybrid waves are generated at the separatrix. In the laboratory, high-power laser experiments have demonstrated electron acceleration from reflected ions in analogy to the solar wind interacting with a comet.[27]

While many acceleration mechanisms may be operating in astrophysical environments, laboratory experiments offer the advantage of tailoring plasma conditions to probe individual mechanisms. The objective of this paper is to model experiments that measure ion

acceleration in a stochastic magnetized plasma at the GSI Helmholtz Centre for Heavy Ion Research facility.[28] We use a platform similar to that fielded previously to study fluctuation dynamo,[29–34] coupled with the UNIversal Linear ACcelerator (UNILAC) of the GSI to launch well-characterized ions through a stochastic magnetic field. Utilizing the radiation-magneto-hydrodynamic (MHD) code FLASH, and the particle-in-cell (PIC) code OSIRIS, we calculate the plasma conditions along the calcium–ion flight path. From the plasma conditions achieved, we can estimate the efficiency of the various acceleration mechanisms and identify the dominant one. Experimental results from a campaign were used to validate the predictive capabilities of the FLASH code.

In Sec. II, we explain the platform employed at the GSI Helmholtz Centre as well as the initialization of the FLASH simulation. Section III describes the simulation results, the temporal evolution of the plasma, plasma conditions achieved, and compares the simulated results to the experiment results. In Sec. IV, we estimate energization of the UNILAC ions from the plasma conditions obtained.

II. EXPERIMENTAL AND SIMULATION CONFIGURATIONS

A. Experimental configuration

The experimental campaign was carried out at the GSI Helmholtz Institute for Heavy Ion research in Darmstadt, Germany, to observe ion acceleration in a stochastic magnetic field. The experimental configuration is shown in Fig. 1. Two $20\,\mu m$ thick, 1 mm diameter CH foils are separated by 1.95 mm. These foils are machined to have a grooved pattern on their inner surface, facing the opposing targets. The grooves consist of ridges $10\,\mu m$ in height, which are $20\,\mu m$ wide, with a $60\,\mu m$ spacing between them.

Two lasers, NHELIX (Nanosecond High Energy Laser for Ion beam eXperiments) and PHELIX (Petawatt High-Energy Laser for Heavy Ion EXperiments), are used to ablate two targets and form a
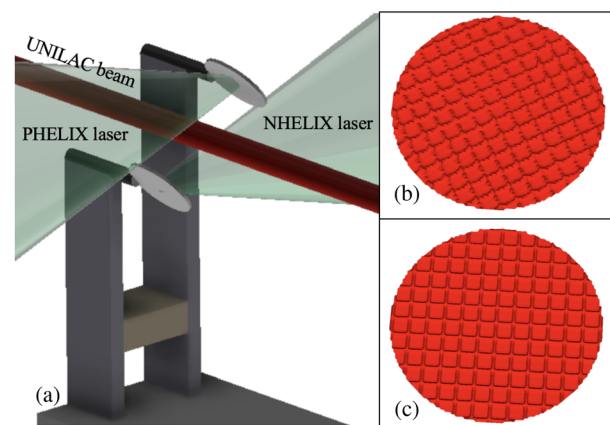
FIG. 1. A diagram of the experimental design fielded at the GSI Helmholtz Institute for Heavy Ion Research. (a) A CAD rendering of target configuration, with two grooved targets separated by 1.95 mm. PHELIX and NHELIX beams, depicted in green, impinge the inner target faces. The UNILAC ion beam, shown in red, has a diameter of $100\,\mu m$, forming a cylinder that intersects the center of the domain between the targets. (b) The upper target's grooved surface, demonstrating the $10\,\mu m$ tall, $20\,\mu m$ wide, $60\,\mu m$ spaced ridges. (c) The lower target's grooved surface demonstrates the groove offset and rotation.

colliding plasma. The UNILAC generates Ca^{+18} ions with an energy of 242 MeV (5.052 MeV per nucleon) and spread in energy of 0.1%. The ions are directed through the center of the experimental chamber, between the two targets, forming a 100 μm diameter, traveling into a diamond detector on the other side of the chamber (see also Fig. 1). An optical spectroscopy diagnostic collects light from over a path integrated area with a 4.0 mm diameter, encompassing the two target, to measure electron density, electron temperature, and the RMS (root mean square) velocity.

B. FLASH configuration

To model this experiment, we utilized the FLASH code. FLASH[35,36] is a publicly available, high-performance computing, multi-physics, adaptive mesh refinement (AMR), finite-volume Eulerian hydrodynamics and MHD code.[37] FLASH has extensive high-energy-density physics (HEDP) capabilities[36] incorporated in recent years, which enable it to model laser–plasma experiments. HEDP experiments typically cannot be described by a thermal equilibrium between electrons, ions, and radiation. Therefore, we employ a three-temperature (3T) description to solve the extended radiation–MHD equations that describe our system. We also leverage other capabilities in FLASH, such as laser ray-tracing, radiation diffusion, and multi-material equation of state (EOS) and opacities. For a detailed explanation, see Tzeferacos et al.[36,38]

The 3D FLASH simulations were configured to replicate the experiments. The simulation domain extends 1.28 mm in X and Y and 3.84 mm in Z. The domain is resolved with $\sim 6.3 \times 10^6$ cells, with a spacing of 10 μm, which is sufficient to fully resolve the grooves, recesses, and target thickness. Outflow boundary conditions are employed to emulate the large experimental campaign. These boundary conditions fix the gradients of the flow properties to zero, except for the normal component of the magnetic field, which is set through the solenoidality condition. The multi-group, flux-limited radiation diffusion scheme uses six energy groups that range from 0.1 eV to 100 keV. For heat exchange, magnetic resistivity, and electron thermal conductivity, the Spitzer formula are used.[39] The generation of the magnetic field is modeled using a generalized Ohm's law, which includes the resistive and Biermann-battery terms.[40,41]

Two CH foils are initialized in the domain, using the parameters from the experimental platform. To accurately model the EOS and opacity of CH, a PROPACEOS[42] table is used. The density of the material is set to 1.04 g cm^{-3} and the initial temperature is set to room temperature. The remaining computational domain is filled with He at 1.0×10^{-6} g cm^{-3} and room temperature.

The NHELIX and PHELIX beams, each simulated using 10 000 rays, have a Gaussian radial profile with 100 μm Gaussian FWHM (full-width at half-maximum) radius of the focal spot. The PHELIX's laser wavelength is set to 1053 nm, while NHELIX's is set to 1064 nm. The beam power is described by a 3 ns ramp up, 4 ns plateau, and 3 ns ramp down, with a plateau power of 7.85×10^9 W.

III. EVOLUTION OF THE EXPERIMENT

Here, we describe the temporal evolution of the experiment as seen in the 3D FLASH simulations. The evolution consists of three distinct phases. Phase I describes the laser ablation of the targets, which generates two fully ionized, counterpropagating jets. Phase II begins when the jets collide between the targets. During this phase, 1D

OSIRIS and FLASH simulations are employed to assess the impact of kinetic effects during the formation of the interaction region, which is the region bounded by two reverse shocks. Finally, Phase III describes the temporal evolution and relaxation of the interaction region.

A. Phase I: Jet generation and propagation

The temporal evolution in the simulation is shown in Fig. 2. The inner face of each target is illuminated by a single beam, absorbing laser energy through electron free-free absorption, otherwise known as inverse bremsstrahlung. This results in ablation of the targets, generating two expanding, supersonic, fully ionized, asymmetric jets. The laser–target interaction generates Biermann-battery magnetic fields,[43,44] which are flux-frozen into the expanding jets and advected with the jets into the center of the domain. The jets retain a density variation, as a result of the grooved pattern present on the target surface. The properties of the jets are summarized in Table I. Approximately, 3 ns after the laser is turned on, the jets collide in the center of the domain. Phase I concludes with the collision of the two jets.

B. Phase II: Collision and counterstreaming

While the two jets are well described by a Maxwellian distribution, this function cannot describe the immediately post-collision plasma. The velocity (4.1×10^7 cm s^{-1}) and density (2.2×10^{18} carbon ions/cm^{-3}) at the jet front have an inter-jet carbon-ion mean free path[45] [Eq. (14.12)],

$$l_{\mathrm{mfp}} \simeq 1.1 \left(\frac{A}{12 \text{ amu}} \right)^2 \left(\frac{2U}{8.2 \times 10^7 \text{ cm s}^{-1}} \right)^4$$
$$\times \left(\frac{n_c}{2.2 \times 10^{18} \text{cm}^{-3}} \right)^{-1} \left(\frac{Z}{6} \right)^{-4} \text{cm}, \quad (1)$$

where A is the carbon-ion mass, n_c is the carbon-ion density, Z is the charge of the carbon ions, and U is the jet velocity (which is the jet's relative velocity). Thus, the inter-jet mean free path of the carbon ions is significantly larger than the 1 mm distance the jets can counterpropagate before hitting the opposing target, giving rise to counterstreaming flows. While the initial plasma properties at the jet front yield inter-jet mean free paths larger than the system size, the velocities decrease and densities increase at later times, shortening the inter-jet mean free path. This counterstreaming cannot be accurately modeled in a single-fluid MHD simulation, and, therefore, we need to assess how it affects the formation of the interaction region and how long it will last.

To that end, we execute a 1D OSIRIS[46–48] PIC simulation (which can capture counterstreaming and kinetic effects). These 1D simulations will result in a longer counterstreaming time than a 3D case, thus giving an upper bound on the counterstreaming phase. The OSIRIS simulation was initialized at the time when the two jets began to merge. Two counterstreaming plasma jets, extending 12.4 mm, were initialized with spatially varying density and velocity profiles in the 28 mm simulation domain. This setup ensured that the particle and electromagnetic-field boundaries were transparent for the physical region of interest (the central 2 mm, or -1 mm $< z < 1$ mm, region). By fine-tuning the density and velocity spatial profiles in the OSIRIS simulation, the time-varying density and velocity profiles of the inflowing plasma jets at $z = \pm 1$ mm were matched to those in the FLASH
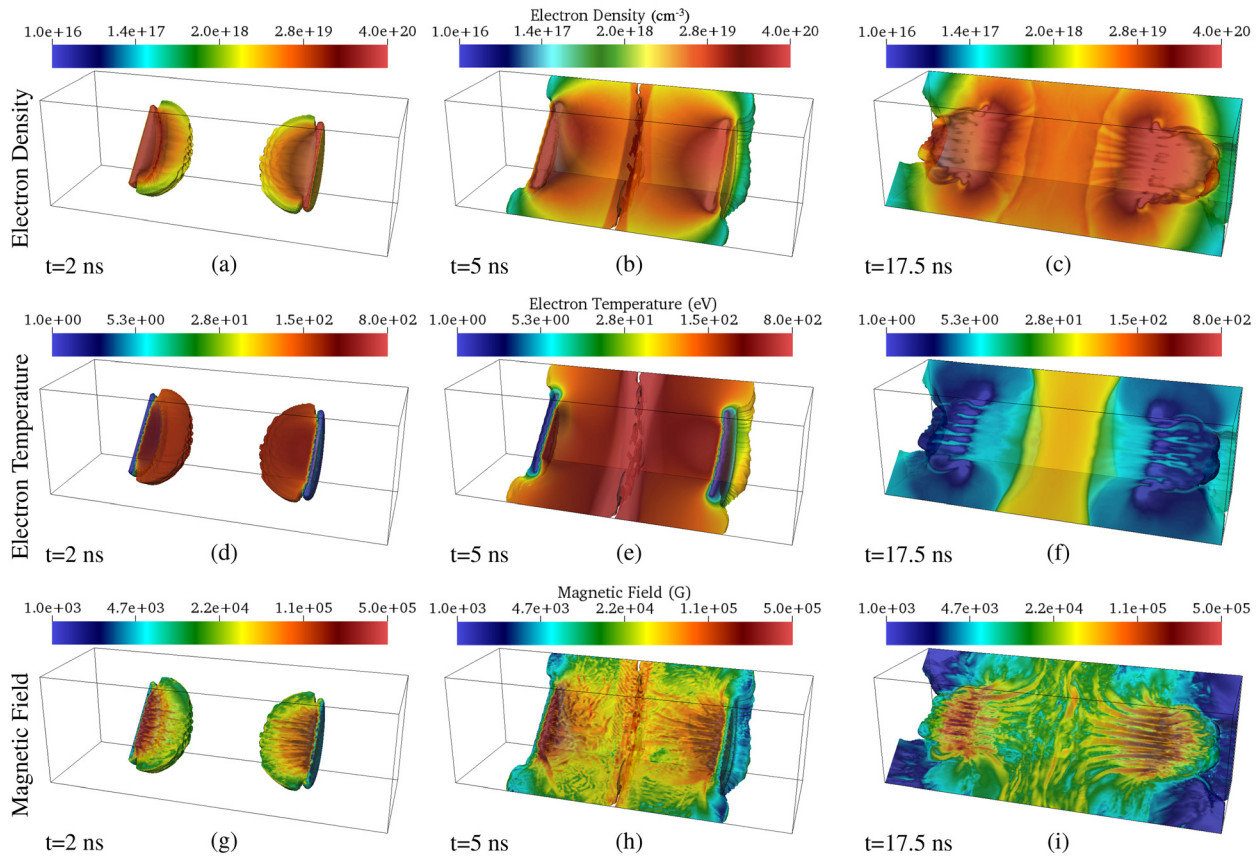
FIG. 2. The time history of the FLASH simulations. The top row shows the temporal evolution of the electron density, the middle row shows the temporal evolution of the electron temperature, and the bottom row shows the temporal evolution of the magnetic field. (a) Rendering of the electron density at $t = 2$ ns. In this visualization, the volume is cut diagonally from the bottom front corner to the top back corner. The grid structure can be seen at the front of the jet as it expands toward the center of the domain. As time progresses, the jets collide in the center and the electron density increases, reaching $\sim 2.5 \times 10^{19}$ cm^{-3} (b). At later times, the beams have been turned off and the density of the material in the center has reduced to $\sim 2.0 \times 10^{19}$ cm^{-3} (c). (d) Rendering of the electron temperature at $t = 2$ ns. The initial jets have temperatures ~ 400 eV. As the jets propagate and collide in the center, forming the interaction region (the region bounded by two reverse shocks), their temperature increases to over 500 eV (e). At later times, the material has cooled down to tens of electron volts (f). (g) Rendering of the magnetic field at $t = 2$ ns. The magnetic field is generated through Biermann-battery laser–target interaction and is advected toward the center of the domain with the plasma flow. As the magnetic field reaches the center of the domain, it is flux-compressed and increased by $\sim 15\%$ (h). At later times, the magnetic field strength in the interaction region is higher than in the surrounding region, but lower than what was observed at earlier times (i).

simulation. Within the 10 ns simulation time, the inflowing jet velocity decreases from 6×10^7 to 6×10^6 cm s^{-1}; the jet density increases from 3×10^{18} to 6×10^{18} cm^{-3}. The grid size of the OSIRIS simulation was set to 3.9×10^{-5} mm, resolving the Debye length for the initial temperature. The numbers of particle-per-cell (PPC) for the three species, namely, electron, carbon, and hydrogen, were 28, 24, and 4, respectively. The choice of PPC numbers ensures the same numerical weight of the charge for all particles, and thus conserves energy and momentum for every binary collision event that is modeled by the collision package[49] in OSIRIS. In Fig. 3, we show a composite image of the jet properties from the OSIRIS PIC simulation. The interpenetration is captured in Fig. 3(a), evidenced by the net positive velocity of all particles that constitute the left jet. However, at 4 ns post-collision [Fig. 4(b)], the interaction region has stagnated at the center of the domain. A comparison of the density to the FLASH code [Fig. 3(c)] shows similar interaction regions at 3 ns. Note that the particle

interpenetration is confined to the 1.5 mm region in the PIC simulations, indicating that the particles are bound between the 2.0 mm region between the two targets.

To build confidence in the 3D FLASH results, which cannot capture the short-lived counterstreaming phase, we compare 1D FLASH simulations with 1D OSIRIS simulations to assess how discrepant the plasma properties are in the interaction region. The 1D FLASH run is initialized in an identical manner as is done in the OSIRIS simulations. In Fig. 4, we compare the temporal evolution of the average electron density over a 100 μm region around the center of the computational domains. Initially the electron density is higher in the FLASH calculations, as the jet is immediately stopped and cannot counterstream. However, by 2 ns FLASH and OSIRIS predict similar densities. This result suggests that while the two codes compute different plasma conditions when the flows are counterstreaming, they quickly converge to similar values. Comparing the size of the interaction region shows a

TABLE I. Simulated plasma properties prior to collision and post-collision.

Plasma property	Formula	Prior to collision[a]	Post-collision[b]
Electron density ρ (cm^{-3})	$\cdots$	2.2×10^{19}	5.0×10^{19}
Ion density n_i (cm^{-3})	$\cdots$	6.7×10^{18}	1.4×10^{19}
Electron temperature T_e (eV)	$\cdots$	391	584
Ion temperature T_i (eV)	$\cdots$	412	536
Average ionization Z	$\cdots$	~ 3.5	~ 3.5
Average atomic mass A	$\cdots$	~ 6.5	~ 6.5
Flow velocity u (cm s^{-1})[c]	$\cdots$	4.1×10^7	0.99×10^7
Reynolds length L (cm)[d]	$\cdots$	0.1	0.008
RMS magnetic field B (G)	$\cdots$	3.8×10^4	1.8×10^5
Coulomb logarithm $\log \Lambda$	$23.5 - \log(n_e^{1/2} T_e^{-5/4}) - \sqrt{10^{-5} + \dfrac{(\log(T_e) - 2)^2}{16}}$	8.35	7.2
Sound speed C_s (cm s^{-1})	$9.80 \times 10^5 \dfrac{(ZT_e + (5/3)T_i)^{1/2}}{A^{1/2}}$	1.2×10^7	1.3×10^7
Mach number M	u/c_s	3.41	0.76
Fluid Reynolds number Re	$uL/\nu \left(\nu = 1.92 \times 10^{19} \dfrac{T_i^{5/2}}{A^{1/2} Z^4 n_i \log \Lambda} \right)$	46,174	205
Magnetic Reynolds number Rm	$uL/\eta \left(\eta = 3.2 \times 10^5 \dfrac{Z \log \Lambda}{T_e^{3/2}} \right)$	2,544	36
Magnetic Prandtl number Pm	Rm/Re	0.055	0.18

[a]Properties in the individual jets before collision.
[b]Properties in the interaction region 10 ns post-collision.
[c]Prior to collision the flow velocity is the bulk flow, while post-collision RMS velocity is used.
[d]Prior to collision, half of the distance between targets is used, while after collision, the ridge + well width is used.

smaller interaction region at first in the FLASH results, as expected. At 3 ns, the two simulations yield interaction regions of similar size as well.

C. Phase III: Relaxation of the interaction region

At this stage, the density has increased in the center of the domain resulting in a developed interaction region whose properties are summarized in Table I. The interaction region is subsonic and expands radially. Because the inflowing plasma jets retain the variations from the grooved pattern, their interaction results in shear and stochastic fluctuations in the interaction region. While the plasma jets continue to flow toward the interaction region, at 7 ns, the laser power ramps down and turns off at 10 ns, leading to a reduction in the density, temperature, and velocity. As the simulation progresses, the plasma temperature in the center reduces from hundreds to tens of electron volts, while the electron density drops from 5×10^{19} to 2×10^{19} cm^{-3}.

D. Magnetic field amplification

The laser–target interactions generate large temperature and density gradients, whose cross product gives rise to a Biermann-battery magnetic field. There is no initial or background magnetic field. The magnetic field is characterized by an RMS value of 165 kG and is flux-frozen into the plasma, as seen by the large magnetic Reynolds number (>1000) in Table I. The magnetic field is advected toward the center

of the domain and undergoes some flux compression, which increases its value to $\sim$200 kG.

Flux compression is not the only mechanism that can increase the magnetic field strength. Given the counterstreaming, we need to also consider the Weibel instability.[50] The Weibel instability is a two-stream instability present in nearly homogeneous plasmas with momentum anisotropy. This instability can spontaneously generate or amplify magnetic fields.[44,51,52] Since the FLASH code does not include the Weibel instability, we must assess if Weibel fields are relevant during the formation of the interaction region. To that end, we follow the work done by Ryutov et al.[53,54] We solve the following dispersion relation to obtain the growth rate of the instability Γ:

$$k^2 + \mu \frac{\Gamma + k^2 R}{\Gamma + k^2 V_{se}} + \frac{\Gamma}{\Gamma + V_s k^2} = \frac{k^2}{\Gamma(\Gamma + V_b k^2) + S k^2}, \quad (2)$$

where

$$\mu = \frac{A m_p}{Z m_e}; \quad R = \frac{\omega_{pi} c}{4\pi u \sigma}; \quad V_{se} = \frac{\eta_{se} \omega_{pi}}{uc}$$
$$V_{b,s} = \frac{\eta_{b,s} \omega_{pi}}{uc}; \quad S = \frac{c_s^2}{u^2}, \quad (3)$$

[see also Eqs. (18) and (19) in Ryutov et al.[53]]. A is the carbon-ion atomic number, m_p is the proton mass, Z is the charge of the carbon ions, m_e is the electron mass, c is the speed of light, u is the velocity of the jets, c_s is the ion sound speed, and η_b and η_s are the bulk and shear viscosities. These parameters are then modified to account for the
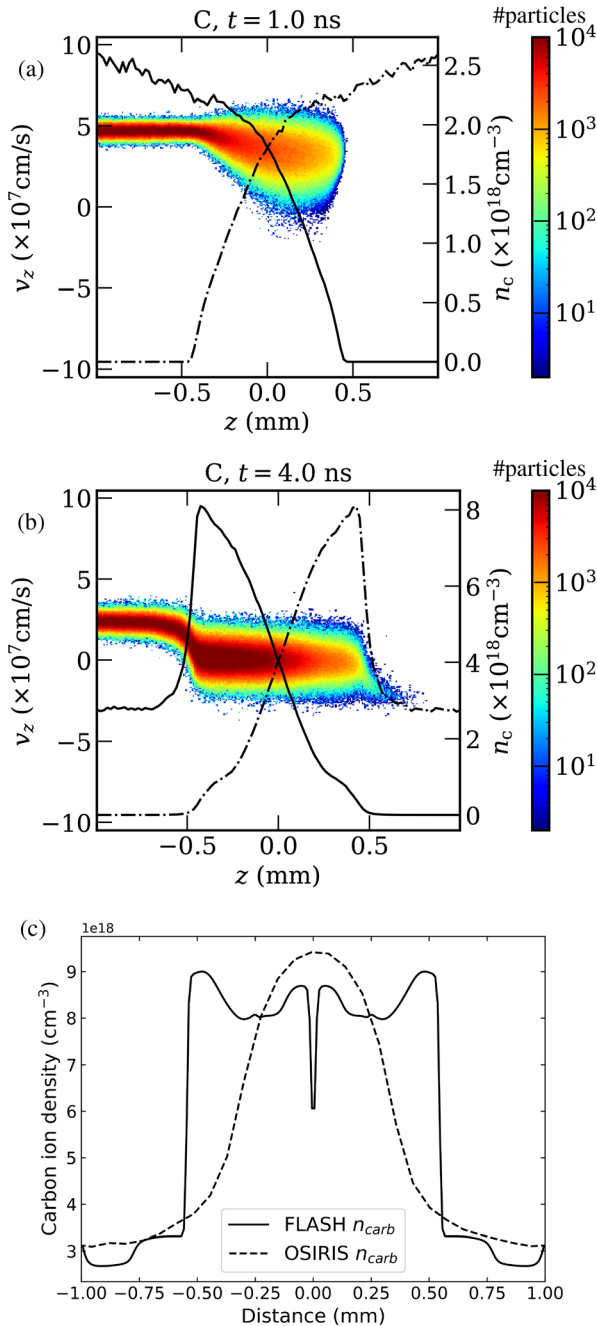
FIG. 3. Time history of the velocity–density map of carbon ions in the OSIRIS PIC simulations, with the solid line representing the density of the left jet and the dotted-dashed line representing the right. (a) The velocity–density map at $t = 1$ ns. The net positive velocity of the particles past the center of the simulation represent the counterstreaming particles of the left jet penetrating the right. While this counterstreaming is initially present, it reduces with time and has fully ended by 4 ns, as the particles stagnate in the center of the domain, shown in panel (b). To compare the formation of the interaction region, we show an overlay of the FLASH 1D carbon density with the OSIRIS 1D results at 3.0 ns in panel (c).
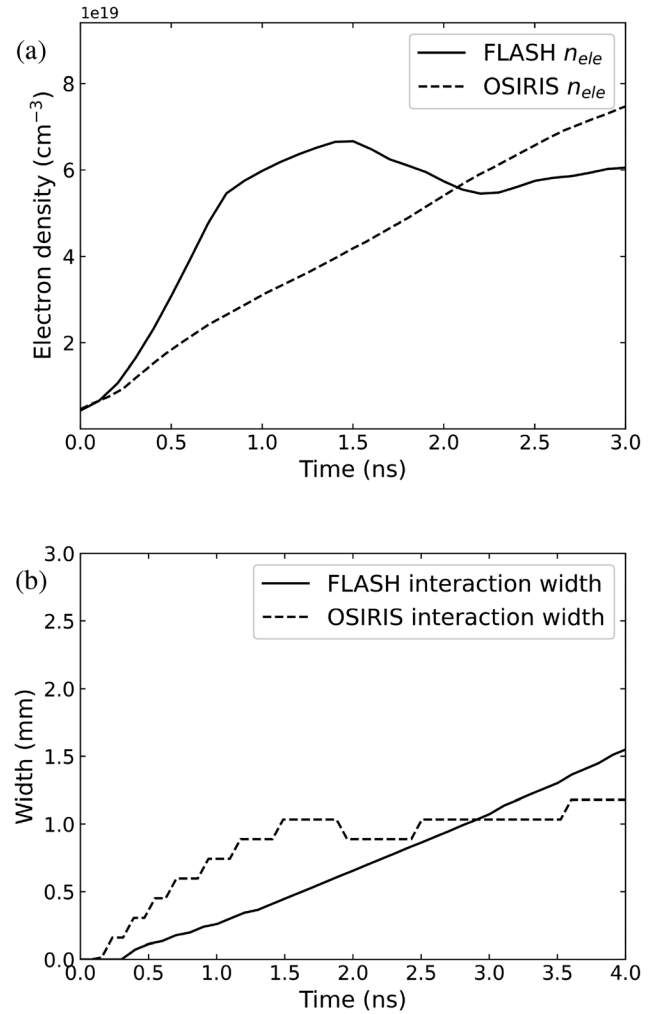
FIG. 4. Comparison of the 1D FLASH (solid line) and OSIRIS (dashed line) simulated properties in the interaction region. The electron density in (a) is averaged over a 100 μm region in the center of the domain. While both simulations are initialized with identical jet parameters, the FLASH calculation initially predicts higher densities that the OSIRIS calculation. As more material accumulates in the center of the domain, the OSIRIS particles stop counterstreaming and accumulate, resulting in a similar value to the FLASH results. Similarly, the plot of the interaction regions width in (b) shows that the interaction width predicted by FLASH is initially smaller, but at $\simeq 3$ ns, the widths match between FLASH and OSIRIS simulations.

addition of hydrogen, following the treatment in Sec. IV (in Ryutov *et al.*[53]) yielding

$$c_s^2 = \frac{5T_i(1 + \alpha)}{3m_p(A_Z + \alpha A_H)}, \tag{4}$$

$$\omega_{pi}^2 = \omega_{pe}^2 \frac{m_e(Z + \alpha)}{m_p(A_Z + \alpha A_H)}, \tag{5}$$

$$\frac{\eta_H}{\eta_Z} \simeq c_H Z^2 \sqrt{\frac{A_H}{A_Z}}, \tag{6}$$

16 December 2024 09:26:15

where α is the number of heavy ions per hydrogen ions, A_H and A_Z are the atomic masses of hydrogen ions and carbon ions, respectively, and ω_{pe} is the electron plasma frequency. With these considerations, we calculate the e-folding time to be ~ 6.7 ns. Given the counter-streaming only occurs for 3 ns in the OSIRIS simulations, the Weibel instability cannot make meaningful contributions to the magnetic field. Therefore, the magnetic field in the interaction region primarily originates from the advected Biermann-battery magnetic field, and not other processes.

E. Validation of plasma properties

We leverage the ongoing experimental campaign to validate the FLASH simulation with optical spectroscopy data. To provide electron density, electron temperature, and a RMS velocity, an optical spectroscopy diagnostic was employed, gathering data over a path integrated area with a 4.0 mm diameter, encompassing the two targets. From this large collection region, a feature in the emitted light, near 470 μm, was fit using PrismSPECT,[55] providing temperature, electron density, and RMS velocity measurements. This peak in the spectra was the only consistent feature across the experimental data and was therefore the one used for the fitting procedure. The error bars on the values were calculated using the 100 best data fits. The uncertainty of the timing of the optical spectroscopy and the fitting procedure only gives approximate values. We therefore present individual values for each plasma property from the experiment, which are representative of the conditions from 15 to 25 ns, shown in Table II under the "Experiment" column. To directly compare experimental and simulation data, we average the FLASH results over a $1.28 \times 1.28 \times 3.84$ mm^3 region (the entire simulation domain), masking for the unablated target. These values are then averaged from 15 to 25 ns, which corresponds to the experimental temporal window when the optical spectroscopy measurement occurred.

The experimental plasma properties and values calculated in the FLASH simulation (under the "Large Volume" column) are shown in Table II. The simulated electron density is within the error bars of the experiment, in good agreement with the spectroscopic data. The ion temperature is somewhat higher than in the experiment, which is due to the lack of the initial counterstreaming in the FLASH simulations, resulting in higher temperature when the two jets collide. This is also why the RMS velocity is somewhat lower in the FLASH simulations, as

more kinetic energy is converted into thermal energy than in the experiment.

The comparison of the FLASH calculations and the experimental results shows agreement over a large volume, but the values of interest for energization are those along the calcium–ion flight path. Employing the FLASH simulations allows us to obtain the plasma conditions and magnetic field of the calcium–ion flight path. Both are required to estimate the ion acceleration and both are different between the large volume and the flight path. Since the FLASH calculations include the magnetic field generation terms and, as shown in Sec. III, the Weibel instability is not expected to affect the magnetic field in the interaction region, we can utilize the properties in the flight path (Table II) to estimate the energization of the calcium ions.

IV. ION ACCELERATION
A. Plasma properties in the ion path

The plasma properties, through a 100 μm diameter and a 1280 μm long cylinder, were calculated, i.e., the calcium–ion flight path. This cylindrical region is in the center of the domain, parallel to the two targets, and the results of averaging over this volume are shown in Fig. 5 (dashed line). As expected, the ions travel through higher densities and temperatures than those measured in the large volume (solid line) region. Conversely, the RMS velocity is lower in the calcium–ion flight path because it does not include the inflowing material. The reduced RMS velocities and increased electron temperature and electron density highlight the need for the FLASH simulations, which show that there is a substantial difference between the large volume and the calcium–ion flight path and will allow a more accurate estimation of particle energization. We calculate the magnetic field in the calcium–ion flight path, finding that it peaks at the 10 ns mark, with a value of 200 kG, dropping to ~ 80 kG by the 15 ns mark, and reduces ~ 50 kG by the 30 ns mark. The calculated plasma properties in the calcium–ion flight path are shown in Table II.

B. Acceleration estimates

The ion beam is not simulated in this work. The reason is two-fold, FLASH cannot accurately capture the plasma and ion–beam interaction and the computational cost associated with running this form of simulation in OSIRIS is prohibitive. Instead scaling laws are used to estimate the particle energization.

TABLE II. Simulated plasma properties in the calcium–ion flight path, large volume, and experimental data. The calcium–ion flight path data are used to estimate the energization.

Plasma property	Calcium–ion flight path	Large volume	Experiment
Electron density ρ (cm^{-3})	2.2×10^{19}	2.1×10^{19}	$1.9 \pm 0.2 \times 10^{19}$
Ion temperature T_i (eV)	96	55	42.1 ± 3.1
Velocity u_{rms} (cm s^{-1})	7.0×10^6	8.1×10^6	$18.1 \pm 2.9 \times 10^6$
Magnetic field B (G)	6.0×10^4	3.5×10^4	$\cdots$
Ion path length L (cm)	0.4	0.4	$\cdots$
Correlation length ℓ_b (cm)	0.013	$\cdots$	$\cdots$
Electron plasma frequency (s^{-1})	2.6×10^{14}	2.5×10^{14}	2.5×10^{14}
Electron gyrofrequency (s^{-1})	1.1×10^{12}	8.8×10^{11}	$\cdots$
Ion plasma frequency (s^{-1})	4.5×10^{12}	4.4×10^{12}	4.2×10^{12}
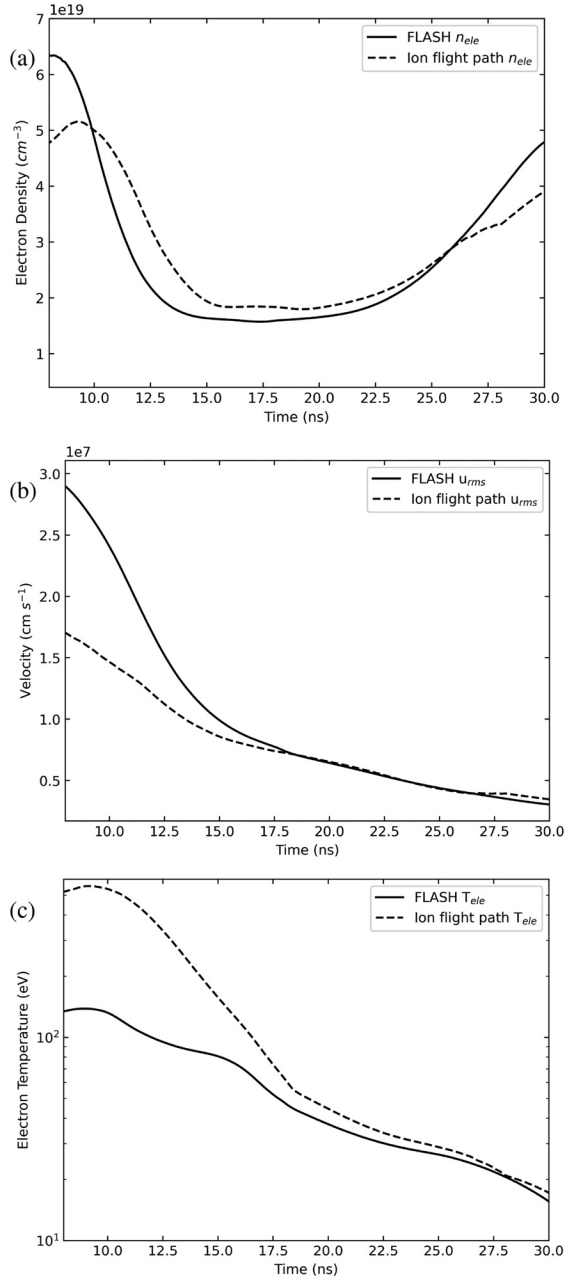
FIG. 5. Simulated plasma properties as functions of time. The simulated plasma properties are averaged over a $1280 \times 1280 \times 3840 \ \mu m^3$ volume (solid line), and the calcium–ion flight path properties are averaged over a $100 \ \mu m$ diameter $\times 1280 \ \mu m$ long cylinder (dashed line). The large volume average excludes the target, using a temperature threshold, but results in an over-inclusion of material initially. (a) Electron density of the simulated plasma over the large volume and small cylinder. For the duration of the simulation, these two values remain similar. (b) RMS velocity of the simulated plasma. The large volume velocity is initially significantly larger as it includes the jets flowing into the interaction region. After the lasers turn off, the solid and dashed lines converge. (c) Electron temperature of the simulated plasma. Initially, the calcium–ion flight path yields significantly higher temperatures, but as the lasers turn off, the temperature begins to drop.

From the late-time plasma conditions that FLASH predicts in the calcium–ion path, we estimate the expected acceleration from first-order and second-order Fermi mechanism, as well as the lower-hybrid drift instability. The time frame of interest is 15–25 ns, i.e., after the interaction region has relaxed to the plasma conditions, also seen in the experiment. These times were chosen as this corresponds to when the ion bunches were launched through the domain in the experiment and is also when the FLASH results match the experiment. To mirror the experimental results, we average the plasma parameters from 15 to 25 ns in the calcium–ion flight path and display them in Table II under the "Calcium–Ion Flight Path" column.

The first-order Fermi mechanism relies on shocks. Since the interaction region is subsonic, and the reverse shocks are outside the calcium–ion path, this mechanism is not expected to contribute to ion acceleration. However, second-order Fermi and lower-hybrid drift can contribute, so we examine each separately.

1. Second-order Fermi acceleration

Second-order Fermi acceleration relies on interactions of particles with magnetic mirrors. In our experiment, this translates to a diffusive acceleration of the calcium ions through magnetic fluctuations [see Figs. 2(g)–2(i)]. To calculate the energy diffusion, we follow a similar calculation by Chen *et al.*[21,31,56,57] The energy change from a single deflection by the magnetic field is

$$\delta\mathscr{E} \sim \frac{Z_c e u_{rms} B_{rms} \ell_b}{c}, \quad (7)$$

where $Z_c e$ is the calcium–ion charge, ℓ_b is the correlation length of the magnetic field,[30] c is the speed of light, and u_{rms} and B_{rms} are the RMS velocity and magnetic field, respectively. As the charged calcium ions traverse the interaction region, they undergo a number of such deflections, which results in a diffusion. The resulting change in energy is

$$\Delta\mathscr{E} \sim \frac{Z_c e u_{rms} B_{rms} \ell_b \sqrt{N_0}}{c}, \quad (8)$$

where N_0 is the number of deflections. This can be approximated as $N_0 \sim L/\ell_b$, where L is the distance the calcium ions travel through. The collisional mean free path of the calcium ions is $l_{mfp} \approx 1.7 \times 10^4$ cm, showing that collisions are not the dominant interactions these particles experience. With this estimate, we find

$$\Delta\mathscr{E} \sim 9.7 \left(\frac{Z_c}{18}\right) \left(\frac{u_{rms}}{7.0 \times 10^6 \, \text{cm s}^{-1}}\right)$$
$$\times \left(\frac{B_{rms}}{60 \, \text{kG}}\right) \left(\frac{L\ell_b}{0.0052 \, \text{cm}^2}\right)^{0.5} \text{keV}. \quad (9)$$

Using the plasma conditions and magnetic field obtained from the FLASH simulations, we estimate the energization the calcium ions would experience to be $\Delta\mathscr{E} \sim 9.7$ keV. Comparing this value to the 0.1% (or 240 keV) energy spread in the generated ions shows that this mechanism will not result in an observable change to the energy spectrum.

2. Lower-hybrid drift instability

The lower-hybrid drift instability is a kinetic instability that generates kinetic waves in a magnetized plasma when there exist gradients

of density and magnetic field.[22,58] These lower-hybrid waves induce an electric field that can accelerate particles. It develops with a growth rate of

$$\gamma = \frac{\sqrt{2\pi}}{8} \frac{v_d^{\,2}}{v_i} \omega_{LH} = 3.4 \times 10^{10}\,\mathrm{s}^{-1}, \tag{10}$$

where v_d is the drift velocity, v_i is the ion velocity, and ω_{LH} is the lower-hybrid frequency. The change in velocity of non-resonant charged particles through a weakly turbulent medium susceptible to this instability can be modeled as a diffusion problem, with the following coefficient:[25,59,60]

$$D_\perp = 2 \frac{Z_c^2}{A_c^2} \frac{\omega_{pi}^2}{\Delta\omega} \frac{W}{nT} c_s^2. \tag{11}$$

Here, Z_c and A_c are the charge and atomic number of the beam ions, ω_{pi} is the ion plasma frequency, $\Delta\omega$ is the bandwidth of the lower-hybrid turbulence (1% of the lower-hybrid frequency was used), W is the wave energy density, nT is the plasma pressure, and c_s is the sound speed. The ratio of electrostatic wave energy density to thermal energy at saturation becomes[58]

$$\frac{W}{nT} \approx 0.05 \left(1 + \frac{\omega_{pe}^2}{\omega_{ce}^2} \right)^{-1}, \tag{12}$$

where ω_{pe} is the electron plasma frequency, and ω_{ce} is the electron gyrofrequency. Using the relation[25] that $D_\perp = |\Delta v|^2 / \tau$, the change in velocity becomes

$$
\begin{aligned}
|\Delta v| &= \sqrt{2 \frac{Z_c^2}{A_c^2} \frac{\omega_{pi}^2}{\Delta\omega} \frac{W}{nT} c_s^2 \frac{L}{v_i}} \\
&= 1.7 \times 10^6 \left(\frac{Z_c}{18} \right) \left(\frac{A_c}{48\,\mathrm{amu}} \right)^{-1} \left(\frac{\omega_{pi}}{4.5 \times 10^{12}\,\mathrm{s}^{-1}} \right) \\
&\quad \times \left(\frac{\Delta\omega}{4.4 \times 10^{10}\,\mathrm{s}^{-1}} \right)^{-0.5} \left(\frac{\frac{W}{nT}}{8.0 \times 10^{-7}} \right)^{0.5} \left(\frac{c_s}{9.0 \times 10^6\,\mathrm{cm\,s^{-1}}} \right) \\
&\quad \times \left(\frac{L}{0.4\,\mathrm{cm}} \right)^{0.5} \left(\frac{v_i}{3.1 \times 10^9\,\mathrm{cm\,s^{-1}}} \right)^{-0.5} \mathrm{cm\,s^{-1}}, \tag{13}
\end{aligned}
$$

where L is the length that the calcium ions traverse, and v_i is the calcium ion velocity. Using the parameters from Table II yields energizations of $\Delta\mathscr{E}$ of 264 keV. This corresponds to a $\sim 0.11\%$ change in energy, which is larger than the calcium ion thermal spread and can be resolved by the available time-of-flight diagnostics.

V. SUMMARY

In this paper, we have shown results of FLASH simulations of a laser-driven experimental campaign at the GSI Helmholtz Institute for Heavy Ion Research, which aims to observe ion acceleration in stochastic magnetic fields. The laser ablation of two targets generates weakly magnetized supersonic jets, which form an interaction region at the center of the chamber. The magnetic field originates from the propagation of the Biermann-battery generated magnetic field from the laser–target interaction. While the Weibel instability may appear in the interaction region during the counterstreaming phase, we found

that its growth rate is too small to have an appreciable effect on the magnetic field.

We validated the simulation results with optical spectroscopy from the experiments and then used the validated FLASH simulations to infer the plasma properties on the calcium–ion flight path. Using the plasma properties calculated using FLASH, we estimated the energization due to second-order Fermi acceleration and lower-hybrid drift instability that would be expected in this experiment. While second-order Fermi acceleration might be acting on the ions, the effect will not be observable. Conversely, the electric field from the lower-hybrid drift instability was found to have a more appreciable effect on the ion energy. The latter is expected to result in energy gains of $\Delta\mathscr{E} \sim 264$ keV, which can be resolved by the time-of-flight diagnostics at the GSI.

AUTHOR DECLARATIONS
Conflict of Interest

The authors have no conflicts to disclose.

Author Contributions

K. Moczulski: Data curation (equal); Formal analysis (equal); Investigation (equal); Methodology (equal); Software (equal); Validation (equal); Visualization (equal); Writing – original draft (equal); Writing – review & editing (equal). **H. Wen:** Conceptualization (equal); Investigation (equal); Resources (equal); Software (equal); Validation (equal); Visualization (equal); Writing – review & editing (equal). **T. Campbell:** Formal analysis (equal); Investigation (equal). **A. Scopatz:** Investigation (equal); Methodology (equal); Writing – original draft (equal); Writing – review & editing

(equal). **C. A. J. Palmer:** Investigation (equal); Writing – review & editing (supporting). **A. F. A. Bott:** Conceptualization (equal); Investigation (supporting); Methodology (supporting); Writing – review & editing (supporting). **C. D. Arrowsmith:** Investigation (supporting); Writing – review & editing (supporting). **K. A. Beyer:** Writing – review & editing (equal). **A. Blazevic:** Investigation (equal). **V. Bagnoud:** Investigation (equal). **S. Feister:** Conceptualization (supporting); Writing – review & editing (supporting). **J. Halliday:** Methodology (supporting); Writing – review & editing (supporting). **O. Karnbach:** Writing – review & editing (supporting). **M. Metternich:** Investigation (supporting). **H. Nazary:** Investigation (equal); Methodology (equal). **P. Neumayer:** Investigation (supporting). **A. Reyes:** Investigation (supporting); Methodology (supporting). **E. C. Hansen:** Investigation (supporting); Methodology (supporting). **D. Schumacher:** Investigation (equal). **C. Spindloe:** Conceptualization (supporting); Investigation (supporting). **S. Sarkar:** Conceptualization (supporting); Writing – review & editing (supporting). **A. R. Bell:** Conceptualization (equal); Methodology (equal). **R. Bingham:** Conceptualization (supporting); Formal analysis (equal); Investigation (equal); Writing – review & editing (supporting). **F. Miniati:** Conceptualization (supporting). **A. A. Schekochihin:** Conceptualization (supporting); Writing – review & editing (supporting). **B. Reville:** Writing – review & editing (supporting). **D. Q. Lamb:** Conceptualization (supporting). **G. Gregori:** Conceptualization (equal); Investigation (supporting); Methodology (supporting); Writing – review & editing (supporting). **P. Tzeferacos:** Conceptualization (equal); Formal analysis (supporting); Funding acquisition (equal); Investigation (supporting); Methodology (supporting); Project administration (equal); Resources (equal); Software (equal); Supervision (equal); Validation (supporting); Visualization (supporting); Writing – original draft (equal); Writing – review & editing (equal).

DATA AVAILABILITY

The data that support the findings of this study are available from the corresponding author upon reasonable request.

REFERENCES

[1]V. Hess, "Über beobachtungen der durchdringenden strahlung bei sieben freiballonfahrten," Phys. Z. **13**, 1084 (1912).

[2]J. Beatty and S. Westerhoff, "The highest-energy cosmic rays," Annu. Rev. Nucl. Part. Sci. **59**, 319–345 (2009).

[3]B. Acharya, I. Agudo, I. Samarai, R. Alfaro, J. Alfaro, C. Alispach, R. Alves Batista, J. Amans, E. Amato, and G. Ambrosi, *Science with the Cherenkov Telescope Array* (World Scientific, 2020).

[4]R. Blandford and D. Eichler, "Particle acceleration at astrophysical shocks: A theory of cosmic ray origin," Phys. Rep. **154**, 1–75 (1987).

[5]W. Axford, E. Leer, and G. Skadron, "The acceleration of cosmic rays by shock waves," Int. Cosmic Ray Conf. **11**, 132–138 (1978).

[6]R. D. Blandford and J. P. Ostriker, "Particle acceleration by astrophysical shocks," Astrophys. J. **221**, L29–L32 (1978).

[7]G. F. Krymskii, "A regular mechanism for the acceleration of charged particles on the front of a shock wave," Akademiia Nauk SSSR Dokl. **234**, 1306–1308 (1977).

[8]A. R. Bell, "The acceleration of cosmic rays in shock fronts - I," Mon. Not. R. Astron. Soc. **182**, 147–156 (1978).

[9]A. Marcowith, A. Bret, A. Bykov, M. E. Dieckman, L. O. Drury, B. Lembege, M. Lemoine, G. Morlino, G. Murphy, and G. Pelletier, "The microphysics of collisionless shock waves," Rep. Prog. Phys. **79**, 046901 (2016).

[10]M. Oka, L. B. Wilson III, T. D. Phan, A. J. Hull, T. Amano, M. Hoshino, M. R. Argall, O. L. Contel, O. Agapitov, D. J. Gershman, Y. V. Khotyaintsev, J. L. Burch, R. B. Torbert, C. Pollock, J. C. Dorelli, B. L. Giles, T. E. Moore, Y. Saito, L. A. Avanov, W. Paterson, R. E. Ergun, R. J. Strangeway, C. T. Russell, and P. A. Lindqvist, "Electron scattering by high-frequency whistler waves at Earth's bow shock," Astrophys. J. Lett. **842**, L11 (2017).

[11]A. J. Hull, L. Muschietti, O. Le Contel, J. C. Dorelli, and P. A. Lindqvist, "MMS observations of intense whistler waves within Earth's supercritical bow shock: Source mechanism and impact on shock structure and plasma transport," J. Geophys. Res.: Space Phys. **125**, e27290 (2020).

[12]O. Agapitov, V. Krasnoselskikh, M. Balikhin, J. Bonnell, F. Mozer, and L. Avanov, "Energy repartition and entropy generation across the earth's bow shock: Mms observations," Astrophys. J. **952**, 154 (2023).

[13]F. Fiuza, G. F. Swadling, A. Grassi, H. G. Rinderknecht, D. P. Higginson, D. D. Ryutov, C. Bruulsema, R. P. Drake, S. Funk, S. Glenzer, G. Gregori, C. K. Li, B. B. Pollock, B. A. Remington, J. S. Ross, W. Rozmus, Y. Sakawa, A. Spitkovsky, S. Wilks, and H.-S. Park, "Electron acceleration in laboratory-produced turbulent collisionless shocks," Nat. Phys. **16**, 916–920 (2020).

[14]D. P. Higginson, P. Korneev, C. Ruyer, R. Riquier, Q. Moreno, J. Béard, S. N. Chen, A. Grassi, M. Grech, L. Gremillet, H. Pépin, F. Perez, S. Pikuz, B. Pollock, C. Riconda, R. Shepherd, M. Starodubtsev, V. Tikhonchuk, T. Vinci, E. d'Humières, and J. Fuchs, "Laboratory investigation of particle acceleration and magnetic field compression in collisionless colliding fast plasma flows," Commun. Phys. **2**, 60 (2019).

[15]W. Yao, A. Fazzini, S. Chen, K. Burdonov, P. Antici, J. Béard, S. Bolaños, A. Ciardi, R. Diab, and E. D. Filippov, "Laboratory evidence for proton energization by collisionless shock surfing," Nat. Phys. **17**, 1177–1182 (2021).

[16]E. Fermi, "On the origin of the cosmic radiation," Phys. Rev. **75**, 1169–1174 (1949).

[17]F. C. Jones, "A theoretical review of diffusive shock acceleration," Astrophys. J., Suppl. Ser. **90**, 561 (1994).

[18]V. Petrosian, "Stochastic acceleration by turbulence," Space Sci. Rev. **173**, 535–556 (2012).

[19]A. Wandel, D. Eichler, J. R. Letaw, R. Silberberg, and C. H. Tsao, "Distributed reacceleration of cosmic rays," Astrophys. J. **316**, 676 (1987).

[20]P. Mertsch, "A new analytic solution for 2nd-order Fermi acceleration," J. Cosmol. Astropart. Phys. **12**, 010 (2011).

[21]K. A. Beyer, B. Reville, A. F. A. Bott, H.-S. Park, S. Sarkar, and G. Gregori, "Analytical estimates of proton acceleration in laser-produced turbulent plasmas," J. Plasma Phys. **84**, 905840608 (2018).

[22]R. C. Davidson, "Quasi-linear stabilization of lower-hybrid-drift instability," Phys. Fluids **21**, 1375–1380 (1978).

[23]J. M. Laming, "Accelerated electrons in Cassiopeia A: An explanation for the hard x-ray tail," Astrophys. J. **546**, 1149 (2001).

[24]F. Lavorenti, P. Henri, F. Califano, S. Aizawa, and N. André, "Electron acceleration driven by the lower-hybrid-drift instability - An extended quasilinear model," Astron. Astrophys. **652**, A20 (2021).

[25]R. Bingham, D. A. Bryant, and D. S. Hall, "A wave model for the aurora," Geophys. Res. Lett. **11**, 327–330, https://doi.org/10.1029/GL011i004p00327 (1984).

[26]Z. Z. Chen, H. S. Fu, J. B. Cao, J. Cui, Q. M. Lu, W. Y. Li, X. C. Dong, Y. Xu, Z. Z. Guo, Z. Wang, and Y. Y. Liu, "Magnetospheric multiscale mission observations of lower-hybrid drift waves in terrestrial magnetotail reconnection with moderate guide field and asymmetric plasma density," Astrophys. J. **933**, 208 (2022).

[27]A. Rigby, F. Cruz, B. Albertazzi, R. Bamford, A. R. Bell, J. E. Cross, F. Fraschetti, P. Graham, Y. Hara, P. M. Kozlowski, Y. Kuramitsu, D. Q. Lamb, S. Lebedev, J. R. Marques, F. Miniati, T. Morita, M. Oliver, B. Reville, Y. Sakawa, S. Sarkar, C. Spindloe, R. Trines, P. Tzeferacos, L. O. Silva, R. Bingham, M. Koenig, and G. Gregori, "Electron acceleration by wave turbulence in a magnetized plasma," Nat. Phys. **14**, 475–479 (2018).

[28]V. Bagnoud, B. Aurand, A. Blazevic, S. Borneis, C. Bruske, B. Ecker, U. Eisenbarth, J. Fils, A. Frank, E. Gaul, S. Goette, C. Haefner, T. Hahn, K. Harres, H.-M. Heuck, D. Hochhaus, D. H. H. Hoffmann, D. Javorková, H.-J. Kluge, T. Kuehl, S. Kunzer, M. Kreutz, T. Merz-Mantwill, P. Neumayer, E. Onkels, D. Reemts, O. Rosmej, M. Roth, T. Stoehlker, A. Tauschwitz, B. Zielbauer, D.

16 December 2024 09:26:15

Zimmer, and K. Witte, "Commissioning and early experiments of the PHELIX facility," Appl. Phys. B **100**, 137–150 (2010).

[29] P. Tzeferacos, A. Rigby, A. F. A. Bott, A. R. Bell, R. Bingham, A. Casner, F. Cattaneo, E. M. Churazov, J. Emig, F. Fiuza, C. B. Forest, J. Foster, C. Graziani, J. Katz, M. Koenig, C.-K. Li, J. Meinecke, R. Petrasso, H.-S. Park, B. A. Remington, J. S. Ross, D. Ryu, D. Ryutov, T. G. White, B. Reville, F. Miniati, A. A. Schekochihin, D. Q. Lamb, D. H. Froula, and G. Gregori, "Laboratory evidence of dynamo amplification of magnetic fields in a turbulent plasma," Nat. Commun. **9**, 591 (2018).

[30] A. F. A. Bott, P. Tzeferacos, L. Chen, C. A. J. Palmer, A. Rigby, A. R. Bell, R. Bingham, A. Birkel, C. Graziani, D. H. Froula, J. Katz, M. Koenig, M. W. Kunz, C. Li, J. Meinecke, F. Miniati, R. Petrasso, H.-S. Park, B. A. Remington, B. Reville, J. S. Ross, D. Ryu, D. Ryutov, F. H. Séguin, T. G. White, A. A. Schekochihin, D. Q. Lamb, and G. Gregori, "Time-resolved turbulent dynamo in a laser plasma," Proc. Natl. Acad. Sci. U. S. A. **118**, e2015729118 (2021).

[31] L. E. Chen, A. F. A. Bott, P. Tzeferacos, A. Rigby, A. Bell, R. Bingham, C. Graziani, J. Katz, M. Koenig, C. K. Li, R. Petrasso, H.-S. Park, J. S. Ross, D. Ryu, T. G. White, B. Reville, J. Matthews, J. Meinecke, F. Miniati, E. G. Zweibel, S. Sarkar, A. A. Schekochihin, D. Q. Lamb, D. H. Froula, and G. Gregori, "Transport of high-energy charged particles through spatially intermittent turbulent magnetic fields," Astrophys. J. **892**, 114 (2020).

[32] A. Bott, L. Chen, G. Boutoux, T. Caillaud, A. Duval, M. Koenig, B. Khiar, I. Lantuéjoul, L. Le-Deroff, B. Reville, R. Rosch, D. Ryu, C. Spindloe, B. Vauzour, B. Villette, A. Schekochihin, D. Lamb, P. Tzeferacos, G. Gregori, and A. Casner, "Inefficient magnetic-field amplification in supersonic laser-plasma turbulence," Phys. Rev. Lett. **127**, 175002 (2021).

[33] J. Meinecke, P. Tzeferacos, J. S. Ross, A. F. A. Bott, S. Feister, H.-S. Park, A. R. Bell, R. Blandford, R. L. Berger, R. Bingham, A. Casner, L. E. Chen, J. Foster, D. H. Froula, C. Goyon, D. Kalantar, M. Koenig, B. Lahmann, C. Li, Y. Lu, C. A. J. Palmer, R. D. Petrasso, H. Poole, B. Remington, B. Reville, A. Reyes, A. Rigby, D. Ryu, G. Swadling, A. Zylstra, F. Miniati, S. Sarkar, A. A. Schekochihin, D. Q. Lamb, and G. Gregori, "Strong suppression of heat conduction in a laboratory replica of galaxy-cluster turbulent plasmas," Sci. Adv. **8**, eabj6799 (2022).

[34] A. F. A. Bott, L. Chen, P. Tzeferacos, C. A. J. Palmer, A. R. Bell, R. Bingham, A. Birkel, D. H. Froula, J. Katz, M. W. Kunz, C.-K. Li, H.-S. Park, R. Petrasso, J. S. Ross, B. Reville, D. Ryu, F. H. Séguin, T. G. White, A. A. Schekochihin, D. Q. Lamb, and G. Gregori, "Insensitivity of a turbulent laser-plasma dynamo to initial conditions," Matter Radiat. Extremes **7**, 046901 (2022).

[35] B. Fryxell, K. Olson, P. Ricker, F. Timmes, M. Zingale, D. Lamb, P. MacNeice, R. Rosner, J. Truran, and H. Tufo, "FLASH: An adaptive mesh refinement code for modeling astrophysical thermonuclear flashes," Astrophys. J., Suppl. Ser. **131**, 273 (2000).

[36] P. Tzeferacos, M. Fatenejad, N. Flocke, C. Graziani, G. Gregori, D. Q. Lamb, D. Lee, J. Meinecke, A. Scopatz, and K. Weide, "FLASH MHD simulations of experiments that study shock-generated magnetic fields," High Energy Density Phys. **17**, 24–31 (2015).

[37] D. Lee, "A solution accurate, efficient and stable unsplit staggered mesh scheme for three dimensional magnetohydrodynamics," J. Comput. Phys. **243**, 269–292 (2013).

[38] P. Tzeferacos, A. Rigby, A. Bott, A. R. Bell, R. Bingham, A. Casner, F. Cattaneo, E. M. Churazov, J. Emig, N. Flocke, F. Fiuza, C. B. Forest, J. Foster, C. Graziani, J. Katz, M. Koenig, C.-K. Li, J. Meinecke, R. Petrasso, H.-S. Park, B. A. Remington, J. S. Ross, D. Ryu, D. Ryutov, K. Weide, T. G. White, B. Reville, F. Miniati, A. A. Schekochihin, D. H. Froula, G. Gregori, and D. Q. Lamb, "Numerical modeling of laser-driven experiments aiming to demonstrate magnetic field amplification via turbulent dynamo," Phys. Plasmas **24**, 041404 (2017).

[39] L. Spitzer, *Physics of Fully Ionized Gases* (Interscience Publishers, 1962).

[40] M. Fatenejad, A. R. Bell, A. Benuzzi-Mounaix, R. Crowston, R. P. Drake, N. Flocke, G. Gregori, M. Koenig, C. Krauland, D. Lamb, D. Lee, J. R. Marques, J. Meinecke, F. Miniati, C. D. Murphy, H. S. Park, A. Pelka, A. Ravasio, B. Remington, B. Reville, A. Scopatz, P. Tzeferacos, K. Weide, N. Woolsey, R. Young, and R. Yurchak, "Modeling HEDLA magnetic field generation experiments on laser facilities," High Energy Density Phys. **9**, 172–177 (2013).

[41] C. Graziani, P. Tzeferacos, D. Lee, D. Q. Lamb, K. Weide, M. Fatenejad, and J. Miller, "The Biermann catastrophe in numerical magnetohydrodynamics," Astrophys. J. **802**, 43 (2015).

[42] J. J. MacFarlane, I. E. Golovkin, and P. R. Woodruff, "HELIOS-CR – A 1-D radiation-magnetohydrodynamics code with inline atomic kinetics modeling," J. Quant. Spectrosc. Radiat. Transfer **99**, 381–397 (2006).

[43] L. Biermann, "Über den ursprung der magnetfelder auf sternen und im interstellaren raum (miteinem Anhang von A. Schlüter)," Z. Naturforsch., A **5**, 65 (1950).

[44] G. Gregori, B. Reville, and F. Miniati, "The generation and amplification of intergalactic magnetic fields in analogue laboratory experiments with high power lasers," Phys. Rep. **601**, 1–34 (2015).

[45] B. A. Trubnikov, "Particle interactions in a fully ionized plasma," Rev. Plasma Phys. **1**, 105 (1965).

[46] R. A. Fonseca, J. Vieira, F. Fiuza, A. Davidson, F. S. Tsung, W. B. Mori, and L. O. Silva, "Exploiting multi-scale parallelism for large scale numerical modelling of laser wakefield accelerators," Plasma Phys. Controlled Fusion **55**, 124011 (2013).

[47] R. A. Fonseca, S. F. Martins, L. O. Silva, J. W. Tonge, F. S. Tsung, and W. B. Mori, "One-to-one direct modeling of experiments and astrophysical scenarios: Pushing the envelope on kinetic plasma simulations," Plasma Phys. Controlled Fusion **50**, 124034 (2008).

[48] R. A. Fonseca, L. O. Silva, F. S. Tsung, V. K. Decyk, W. Lu, C. Ren, W. B. Mori, S. Deng, S. Lee, T. Katsouleas, and J. C. Adam, "OSIRIS: A three-dimensional, fully relativistic particle in cell code for modeling plasma based accelerators," Lect. Notes Comput. Sci. **2331**, 342–351 (2002).

[49] T. Takizuka and H. Abe, "A binary collision model for plasma simulation with a particle code," J. Comput. Phys. **25**, 205–219 (1977).

[50] E. S. Weibel, "Spontaneously growing transverse waves in a plasma due to an anisotropic velocity distribution," Phys. Rev. Lett. **2**, 83–84 (1959).

[51] C. Davidson, Z.-M. Sheng, T. Wilson, and P. McKenna, "Theoretical and computational studies of the Weibel instability in several beam–plasma interaction configurations," J. Plasma Phys. **88**, 905880206 (2022).

[52] C. M. Huntington, F. Fiuza, J. S. Ross, A. B. Zylstra, R. P. Drake, D. H. Froula, G. Gregori, N. L. Kugland, C. C. Kuranz, M. C. Levy, C. K. Li, J. Meinecke, T. Morita, R. Petrasso, C. Plechaty, B. A. Remington, D. D. Ryutov, Y. Sakawa, A. Spitkovsky, H. Takabe, and H.-S. Park, "Observation of magnetic field generation via the Weibel instability in interpenetrating plasma flows," Nat. Phys. **11**, 173–176 (2015).

[53] D. D. Ryutov, F. Fiuza, C. M. Huntington, J. S. Ross, and H.-S. Park, "Collisional effects in the ion Weibel instability for two counter-propagating plasma streams," Phys. Plasmas **21**, 032701 (2014).

[54] D. D. Ryutov, "Rayleigh–Taylor instability in a finely structured medium," Phys. Plasmas **3**, 4336–4345 (1996).

[55] J. J. MacFarlane, I. E. Golovkin, P. R. Woodruff, S. K. Kulkarni, and I. M. Hall, "Simulation of plasma ionization and spectral properties with PrismSPECT," in *IEEE International Conference on Plasma Science (ICOPS)* (IEEE, 2013), p. 1.

[56] A. F. A. Bott, C. Graziani, P. Tzeferacos, T. G. White, D. Q. Lamb, G. Gregori, and A. A. Schekochihin, "Proton imaging of stochastic magnetic fields," J. Plasma Phys. **83**, 905830614 (2017).

[57] D. B. Schaeffer, A. F. Bott, M. Borghesi, K. A. Flippo, W. Fox, J. Fuchs, C. Li, F. H. Séguin, H.-S. Park, P. Tzeferacos, and L. Willingale, "Proton imaging of high-energy-density laboratory plasmas," Rev. Mod. Phys. **95**, 045007 (2023).

[58] J. B. McBride, E. Ott, J. P. Boris, and J. H. Orens, "Theory and simulation of turbulent heating by the modified two stream instability," Phys. Fluids **15**, 2367–2383 (1972).

[59] D. K. Bhadra, C. Chu, R. W. Harvey, and R. Prater, "Studies of radio frequency current drive in a plasma," Plasma Phys. **25**, 361 (1983).

[60] C. S. Liu, V. S. Chan, D. K. Bhadra, and R. W. Harvey, "Theory of runaway-current sustainment by lower-hybrid waves," Phys. Rev. Lett. **48**, 1479–1482 (1982).